Materials Today • Volume xxx, Number xx • xxxx 2021 RESEARCH

ELSEVIER

RESEARCH: Original Research

Hierarchical build-up of bio-based nanofibrous materials with tunable metal–organic framework biofunctionality

Jowan Rostami [1,*], Korneliya Gordeyeva [2], Tobias Benselfelt [1], Ekeram Lahchaichi [1], Stephen A. Hall [3], Anastasia V. Riazanova [1,4], Per A. Larsson [1], Goksu Cinar Ciftci [1,*], Lars Wågberg [1,4,*]

[1] KTH Royal Institute of Technology, Department of Fiber and Polymer Technology, Stockholm, Sweden
[2] KTH Royal Institute of Technology, Department of Engineering Mechanics, Stockholm, Sweden
[3] Lund University, Division of Solid Mechanics, Lund, Sweden
[4] KTH Royal Institute of Technology, Department of Fiber and Polymer Technology, Wallenberg Wood Science Centre (WWSC), Stockholm, Sweden

Multifunctional, light-weight, responsive materials show promise in a range of applications including soft robotics, therapeutic delivery, advanced diagnostics and charge storage. This paper presents a novel, scalable, efficient and sustainable approach for the preparation of cellulose nanofibril-based aerogels *via* a facile ice-templating, solvent exchange and air-drying procedure, which could replace existing inefficient drying processes. These ambient-dried aerogels (~99% porosity) exhibit a high specific compressive modulus (26.8 ± 6.1 kPa m^3 kg^{-1}, approaching equivalence of carbon-nanotube-reinforced aerogels), wet stability and shape recovery (80–90%), favorable specific surface area (90 m^2 g^{-1}) and tunable densities (2–20 kg m^{-3}). The aerogels provide an ideal nanofibrillar substrate for *in-situ* growth of metal–organic frameworks (MOFs), *via* co-assembly of MOF precursors with proteins in aqueous solutions. The resulting hybrid aerogels show a nine-fold increase in surface area (810 m^2g^{-1}), with preserved wet stability and additional protein biofunctionality. The hybrid aerogels facilitate a pH-controlled release of immobilized proteins, following a concomitant disassembly of the surface grown MOFs, demonstrating their use in controlled delivery systems. The colorimetric protein binding assay of the biofunctionalized hybrid aerogel also demonstrates the potential of the material as a novel 3D bioassay platform, which could potentially be an alternative to plate-based enzyme-linked immunosorbent assay.

Keywords: 3D lightweight materials; Aerogels; Cellulose nanofibrils; Metal–organic frameworks; Controlled release; Protein binding assay

Introduction

Due to rapid contamination of the environment with residues from non-biodegradable materials, demand for the development and production of lightweight multifunctional materials from natural resources has increased drastically. In this respect, aerogels from sustainable resources have turned out to be very promising candidates. Aerogels are highly porous, low-density materials with a dispersing phase comprising of air or gas [1]. These materials have excellent potential for a wide variety of applications, such as lightweight construction [2], thermal insulation [2,3], superabsorbents [4], separation media [5], catalysis [6,7], energy storage [8,9], and many more. Although aerogels

* Corresponding authors.
E-mail addresses: Rostami, J. (jowan@kth.se), Cinar Ciftci, G. (goksucc@kth.se), Wågberg, L. (wagberg@kth.se).

1369-7021/© 2021 The Author(s). Published by Elsevier Ltd. https://doi.org/10.1016/j.mattod.2021.04.013This is an open access article under the CC BY-NC-ND license (http://creativecommons.org/licenses/by-nc-nd/4.0/).

Please cite this article in press as: J. Rostami et al., Materials Today (2021), https://doi.org/10.1016/j.mattod.2021.04.013

have been available since 1931, first being demonstrated by Kistler [10], their commercialization is hampered by the high energy cost and time-demanding processes such as freeze-drying or supercritical drying. In this respect, it is of great scientific importance to explore new preparation routes to prepare bio-based aerogels at larger scales.

Owing to their small cross-section (3–4 nm) and high aspect ratio (~200) [11,12], cellulose nanofibrils (CNFs) form gel networks at low solid contents that can be used in the freeze-linking process to fabricate bio-based aerogels with scale-up potential. In this approach, CNFs are forced together by the growing ice crystals, where the freezing rate and particle concentration control the size of the ice crystals and the overall pore structure of the final material [13,14]. Ice-templating leads to fairly large pores and micrometer thick, interconnected fibrous pore walls that can withstand the capillary pressure during drying under ambient conditions. By using aldehyde-containing CNFs or by the inclusion of alginate and calcium ions, this technique can also produce water-resilient aerogels that do not collapse in water [15–17]. However, there are still limitations in terms of achieving higher specific surface areas (SSA), lack of homogeneity due to temperature and ice-formation gradients during freezing, and in reaching very low-densities (<10 kg m^{-3}) [18].

Nonetheless, the highly porous, wet-resilient structure of CNF-based aerogels is suitable for *in-situ* hierarchical build-up of crystalline, three-dimensional MOFs via coordination-driven self-assembly of inorganic and organic moieties in aqueous solutions [19,20]. MOFs alone are typically synthesized in powder form, which often limits their practical use in different applications [21,22]. However, by incorporating MOFs within a stable and resilient 3D bio-based substrate, many of the crystals' excellent characteristics, such as large specific surface area, thermal stability, high degree of crystallinity, and tunable porosity [23,24], can be advantageously used in different applications, including membrane-based separation [25], water purification [5], gas storage [26], catalysis [27], sensing [28–30], and controlled drug delivery [19].

Zeolitic imidazolate framework-8 (ZIF-8), in which tetrahedral zinc(II) ions are linked through 2-methylimidazole (HMIM) ligands, creating a sodalite (SOD) topology in aqueous solutions [31–33], is one of the most widely studied MOFs [24,34–37]. Different biomacromolecules, such as proteins [38–41], can be incorporated during the *in-situ* ZIF-8 crystal formation by mimicking natural biomineralization processes [38,42]. Importantly, this facile protein immobilization approach can protect the biomolecular functionality in harsh environments [38]. In addition, a release of the incorporated biomolecules can be triggered upon a slight decrease in solution pH, resulting in disassembly of the coordination bonds due to the protonation of the HMIM moieties [19,35,38]. To this end, the incorporation of these high surface area ZIF-8 MOFs within a bio-based porous template is of great scientific and technological interest.

Here we report a new, simple and scalable process of making highly porous (~99% porosity), wet stable, bio-based aerogels *via* air drying, utilizing the binding and dissolution properties of $CaCO_3$ particles. These aerogels have a compressive modulus (26.8 ± 6.1 kPa m^3 kg^{-1}) superior to many other cellulose-based aerogels, as well as having ultra-low densities (2–20 kg/m^3); comparable with e.g. supercritical dried silica aerogels [43–48]. Furthermore, the structural and mechanical merits of the wet-stable CNF-based aerogels make them suitable for creating strong, low-density materials with protein-functionalized MOFs, using a simple, water-based biomimetic co-assembly approach. To demonstrate the potential use of these bio-functional MOF-hybridized aerogels in biomedical applications, controlled release of a model protein was demonstrated using the wet-stable hybrid materials. Moreover, the immobilization of the proteins on the aerogels allows for the development of a proof-of-concept 3D bioassay platform based on a colorimetric enzyme-linked detection strategy.

Results and discussion

Aerogels were prepared by mixing different weight ratios of carboxymethylated CNF gel (Fig. S1), alginate solution, and calcium carbonate ($CaCO_3$) particle suspension with subsequent freezing in a conventional freezer (−18 °C), thawing, solvent exchange, and air drying.

The mutual negative charge of CNFs and alginate enables the formation of a homogenous mixture of polymers and anisotropic cellulose nanoparticles [49]. By incorporating $CaCO_3$ particles into the mixture, wet-stability can be obtained in a post-dissolution process during the solvent exchange procedure. A co-continuous network is then formed, where the CNF network is distributed within a Ca^{2+}-crosslinked network of alginate. To gain an understanding of the surface charge of these particles and their role in the network, the zeta (ζ)-potential of dialyzed $CaCO_3$ particles was measured, yielding a rather low negative value of −9.0 ± 0.5 mV, as seen in Table S1. The use of negatively charged $CaCO_3$ particles further favors the formation of a homogenous mixture between the particles and the anionic CNF-alginate network. In this work, the majority of the $CaCO_3$ particles are observed to be micrometer-sized spherical vaterite polymorphs [50–52], and, to some minor extent, the polymorph calcite. Furthermore, the $CaCO_3$ particles have a rather wide particle size distribution, with diameters ranging from the nanometer scale, up to several micrometers. As seen by the number-based particle diameter distribution of the $CaCO_3$ particles (Fig. S2), there is a large spread of particle sizes in the $CaCO_3$ mixture, with the smallest ones ranging from ~20 nm and above. Moreover, even smaller particles could be present but are indistinguishable due to the higher intensity of larger particles in Dynamic Light Scattering (DLS) measurements.

For the material to withstand the conversion from a hydrogel to an aerogel without collapsing, a strong, dense, and interconnected network is needed, which is achieved in this work by ice templating (Fig. 1a). Upon exposure of the hydrogels to temperatures below the freezing point, ice crystals nucleate and grow, resulting in the densification of the dispersed components in the progressively reducing volume between the ice crystals. Following thawing and solvent exchange, the resultant aerogels (Fig. 1b) have ice-templated pores (Fig. 1c) and lamellar pore-walls (Fig. 1d) corresponding the volume fraction expelled from the ice crystals, all while still maintaining individual, random, in-plane oriented fibrils in the pore walls (Fig. 1e).

Please cite this article in press as: J. Rostami et al., Materials Today (2021), https://doi.org/10.1016/j.mattod.2021.04.013

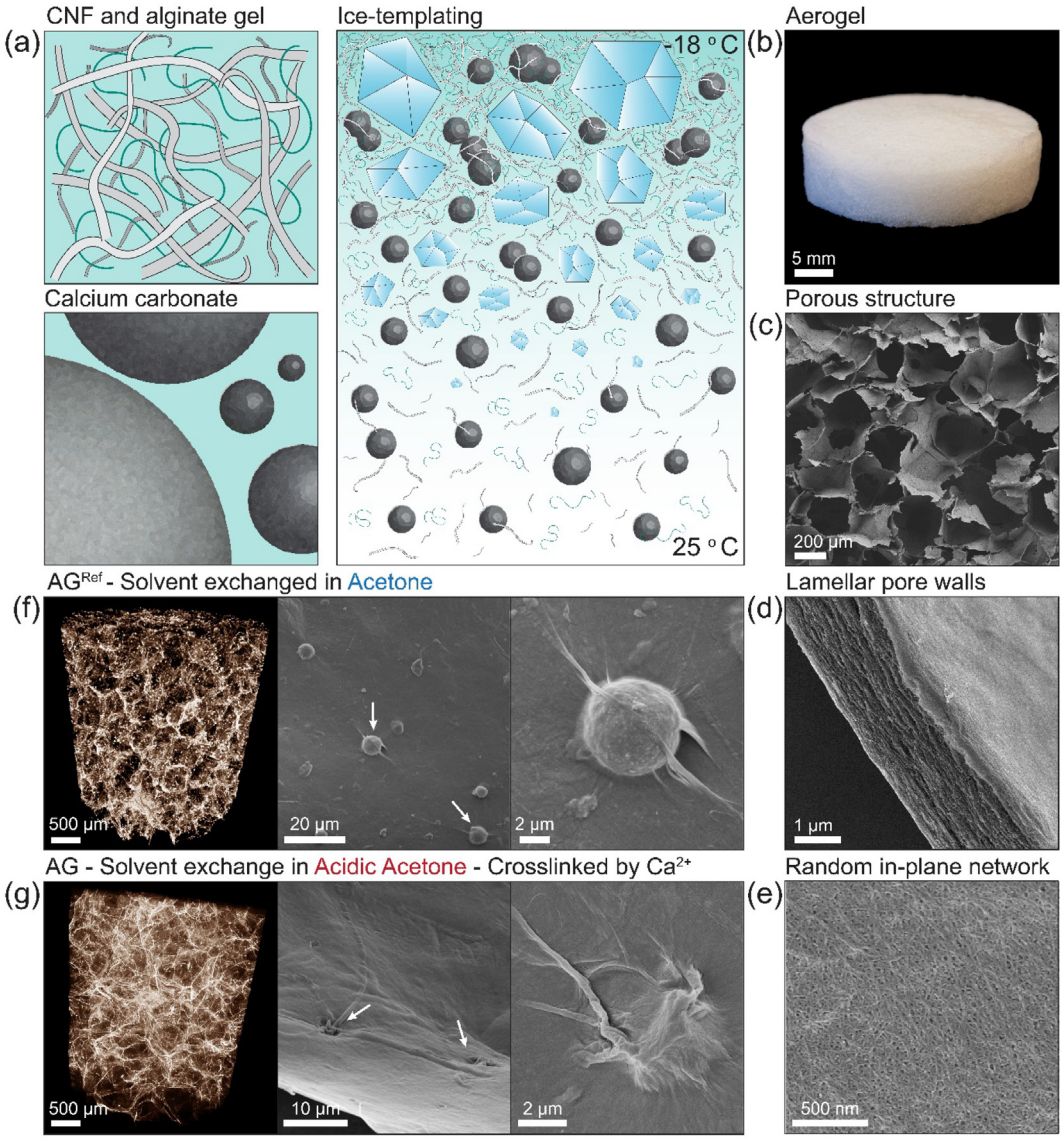

FIGURE 1

Aerogel preparation and structural characteristics. Showing (a) an illustration of the formation of the hydrogel, followed by ice-templating, and (b) a photo of the obtained ambient-dried aerogel, with electron micrographs of its (c) porous structure (d) lamellar pore walls, and (e) random in-plane fibrillar network. The aerogels were obtained either via solvent exchange to (f) acetone (AG^{Ref}), where solid $CaCO_3$ particles are embedded in the CNF-alginate matrix or (g) 10% (w/w) acetic acid in acetone (AG), resulting in the dissolution of the particles and formation of the typical ridges shown in the pictures.

To preserve the hydrogel structure upon solvent removal, capillary forces should be kept as low as possible to avoid a capillary pressure-driven collapse of the network. This was achieved during solvent-exchange, with the combination of a low surface tension solvent that minimized swelling of the fibrillar network and a strong, interconnected network (of mostly cellulose) that was able to withstand air drying of the solvent to form an aerogel. In the case of thawing and solvent exchange to pure acetone (AG^{Ref}), i.e. no acid present in the acetone, the $CaCO_3$ particles remain undissolved and embedded in the CNF-alginate matrix, which can be observed in Fig. 1f, as well as in additional energy-dispersive X-ray spectroscopy (EDS) maps, electron micrographs and microtomography analysis (Figs. S3–S8, Supplementary Video V1). However, if the frozen hydrogel is solvent exchanged with a small amount (10% w/w) of acetic acid in acetone (AG), the $CaCO_3$ particles dissolve to liberate Ca^{2+} ions, which act as an efficient crosslinker of the alginate and CNFs to increase the wet strength of the network [49,53]. Simultaneously, most of the carbonate ions leave the system as carbon dioxide, as bubbles can be observed leaving the network (Supplementary Video V2). This may be an important step in the overall process as it potentially creates an even more open, porous structure. The electron micrographs, EDS maps, and microtomography analysis for AG (as seen in Fig. 1g, Figs. S10–S13, and Supplementary Video V3) indicate that the dissolution of $CaCO_3$ particles leads to the formation of ridges that are remnants of collapsed structures ($CaCO_3$ particles).

After dissolving the $CaCO_3$ particles, the average mass of 10 independent AG aerogels was 11.5 ± 1.0% lower than AG^{Ref} aerogels, which is approximately consistent with the originally incor-

Please cite this article in press as: J. Rostami et al., Materials Today (2021), https://doi.org/10.1016/j.mattod.2021.04.013

porated mass of $CaCO_3$ (12.2% of the total dry weight, before dissolution; Table S3 and S4). Indicating that the loss of mass can be attributed to the dissolution of the particles. This observation is also supported by X-ray diffraction (XRD) analysis. As can be seen in Fig. 2a, the calcite and vaterite polymorph Bragg peaks that are present in AG^{Ref} are not as clearly observed in the XRD pattern for AG, which shows only characteristic cellulose peaks.

The lack of crosslinking in AG^{Ref} is evident as the aerogel disintegrates when immersed in water and exposed to pressure. AG aerogels on the other hand are highly wet stable, as shown from the cyclic wet compression results shown in Fig. 2b. These tests involved soaking two independent AG aerogels in water for at least one hour, followed by three cycles of 80% compression. The compression induced a certain amount of permanent deformation to both AG aerogels, leading to an average shape recovery of 88.0% for the first cycle. For the second and third cycles, the average shape recovery was 84.2% and 82.2%, respectively. The AG aerogels also exhibit remarkable wet shape-recovery after compression at reduced pressure (95 kPa) and elevated temperature (93 °C), followed by re-wetting (as seen in Fig. 2d, Figs. S19–S21, and Supplementary Video V4). This excellent shape recovery also facilitates efficient and environmentally friendly delivery of these types of lightweight materials since transportation of air can be avoided.

To assess the dry mechanical properties of the aerogels, the dry aerogels were left to condition at 23 °C and 50% RH for 48 h before being compressed to 90%. The average specific compressive modulus of the AG aerogels, normalized to the post-conditioned density (19.1 ± 0.7 kg m^{-3}), results in a value of 26.8 ± 6.1 kPa m^3 kg^{-1} (Fig. S22). It is important to note that the mechanical properties of CNF-based materials are strongly influenced by the characteristics of the used CNFs [58], whereby deviations in surface charge and aspect ratio from batch to batch can impact aerogel properties. Thus, AG aerogels prepared using a new batch of CNFs exhibited lower specific compressive modulus (16.2 ± 3.9 kPa m^3 kg^{-1}), most probably as a result of a lower surface charge of the CNFs (448.1 ± 24.7 μmol/g), compared to the earlier measured surface charge of 632.7 ± 48.6 μmol/g. This lower charge potentially leads to a poorer dispersion of the CNFs and hence altered network properties [12].

In comparison, the average specific compressive modulus of AG^{Ref} was 8.2 ± 1.4 kPa m^3 kg^{-1}, when normalized to the post-conditioned density of 21.6 ± 0.3 kg m^{-3} (Fig. S22). The difference in compressive modulus between AG and AG^{Ref} indicates that there is a significant change in the lamellar structure of the pore walls upon dissolution of the incorporated $CaCO_3$ particles. The dissolution of the $CaCO_3$ results in a structure with a lower overall density since $CaCO_3$ has a higher density than the CNFs. Furthermore, if the spherical $CaCO_3$ particles are not present the overall result will be an increase in the compressive properties of the aerogels, when normalized to the aerogel density. The results also clearly indicate that the presence of $CaCO_3$ particles, in the lamellae, decreases the overall compressive properties of the aerogels. This suggests that the particles act as a filler that prevents intimate contact between CNFs in the pore walls and thus do not fully utilize the excellent properties of the nanocellulose. It is also probable that protonation of carboxylic acids with the presence of acetic acid minimizes the swelling of the pore walls during thawing, leading to stiffer pore walls [53].

How Ca^{2+} is introduced to the network also seems to be of large importance. To test and quantify this, two control were prepared with the same parameters as the regular AG, but without the addition of any $CaCO_3$ particles: one with calcium chloride ($CaCl_2$) addition before freezing ($AG^{Pre\text{-}CaCl_2}$), and one with $CaCl_2$

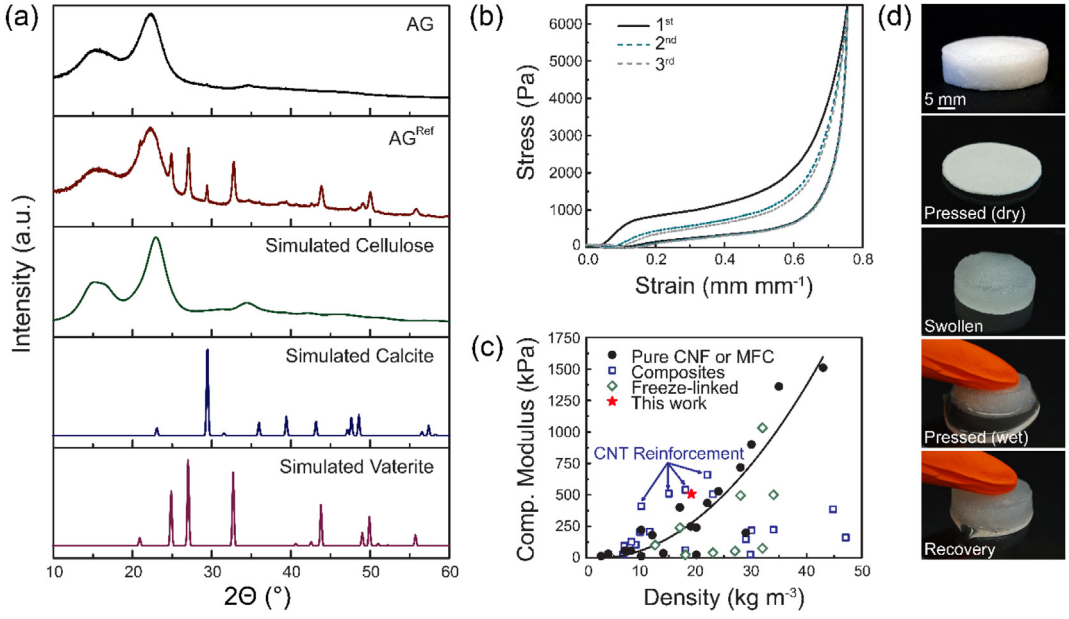

FIGURE 2

Aerogel properties. Showing (a) XRD patterns for AG^{Ref} and AG, (b) wet cyclic (3 cycles) compression for AG, (c) Ashby plot comparing AG with relevant lightweight nanocellulose based materials found in the literature [14,18,54–57], and (d) sequence of photographs showing the ability of wet AG to be compressed at 95 kPa at 93 °C, and then re-wetted to regain its original dimensions.

Please cite this article in press as: J. Rostami et al., Materials Today (2021), https://doi.org/10.1016/j.mattod.2021.04.013

added to the acetone used to thaw the frozen hydrogels ($AG^{Post_CaCl_2}$). For the first control group, the same molar amounts of $CaCl_2$, as compared to the addition of $CaCO_3$, were added to the network before freezing and solvent exchange to acetone. Adding Ca^{2+} before freezing likely leads to uncontrolled aggregation of CNF and alginate, and prevents efficient packing of the components during freezing in the pore walls, which results in the formation of defective structures and an overall significantly lower compressive modulus of 5.6 ± 2.0 kPa m^3 kg^{-1} (Fig. S23).

For the second control group, $CaCl_2$ was added to the acetone during the simultaneous thawing and solvent exchange (for 1 h). In this case, the migration of Ca^{2+} into the pore walls of the material is limited by diffusion and the solubility of $CaCl_2$ in acetone, presumably resulting in an inhomogeneous crosslinking. It should be noted that within the first 10 min of the solvent exchange, all $CaCl_2$ was dissolved, due to the introduction of water from the frozen hydrogels to the acetone. These aerogels performed significantly better than the first control group, with a specific compressive modulus of 14.1 ± 6.2 kPa m^3 kg^{-1}, however not as well as the aerogels in which Ca^{2+} ions are released from incorporated $CaCO_3$ particles.

This indicates that slow and controlled crosslinking from homogeneously incorporated $CaCO_3$ particles results in better mechanical properties and lower densities compared to the other aerogels (Table S5). With apparently bulkier and stiffer pore walls, the overall density of these AG aerogels can be as low as 2 kg m^{-3} (note that the density of air is 1.2 kg m^{-3}) with a minimal collapse of the network (Fig. S24 and Supplementary Video V5. To the best of our knowledge, this is the lowest nanocellulose-based aerogel density reported after air drying or ice-templating, which opens new possibilities in terms of the design of multifunctional lightweight 3D materials.

An interesting effect of the $CaCO_3$ dissolution process is that the SSA, estimated from the Brunauer–Emmet–Teller (BET) model, increased from 10 m^2g^{-1} for AG^{Ref}, that to a large extent exhibits macropores, to 90 m^2g^{-1} for AG, also containing mesopores (Fig. 3c, Fig. S25, and Table S6). The presence of the mesopores in AG samples is most likely a direct consequence of the dissolution of the nanometer-sized $CaCO_3$ particles. Also, during exposure of the frozen hydrogels to 10% (w/w) of acetic acid in acetone, three solvents are present: water, acetic acid, and acetone. During the dissolution process, the CNF and alginate network can re-arrange and "move around", creating new voids and spaces after the dissolution; most probably, this results in a collapse of the voids left by the dissolved particles. Generally, upon freezing, the SSA decreases as the ice crystals densify the fibrillar pore walls and other components, which suggests that the cavities formed following the dissolution of the $CaCO_3$ particles are to a significant extent preserved in the AG, leading to an increased SSA. This is supported by a fitting of the data to the Barrett-Joyner-Halenda (BJH) pore size distribution model in the mesoporous region for AG, showing that the cumulative pore

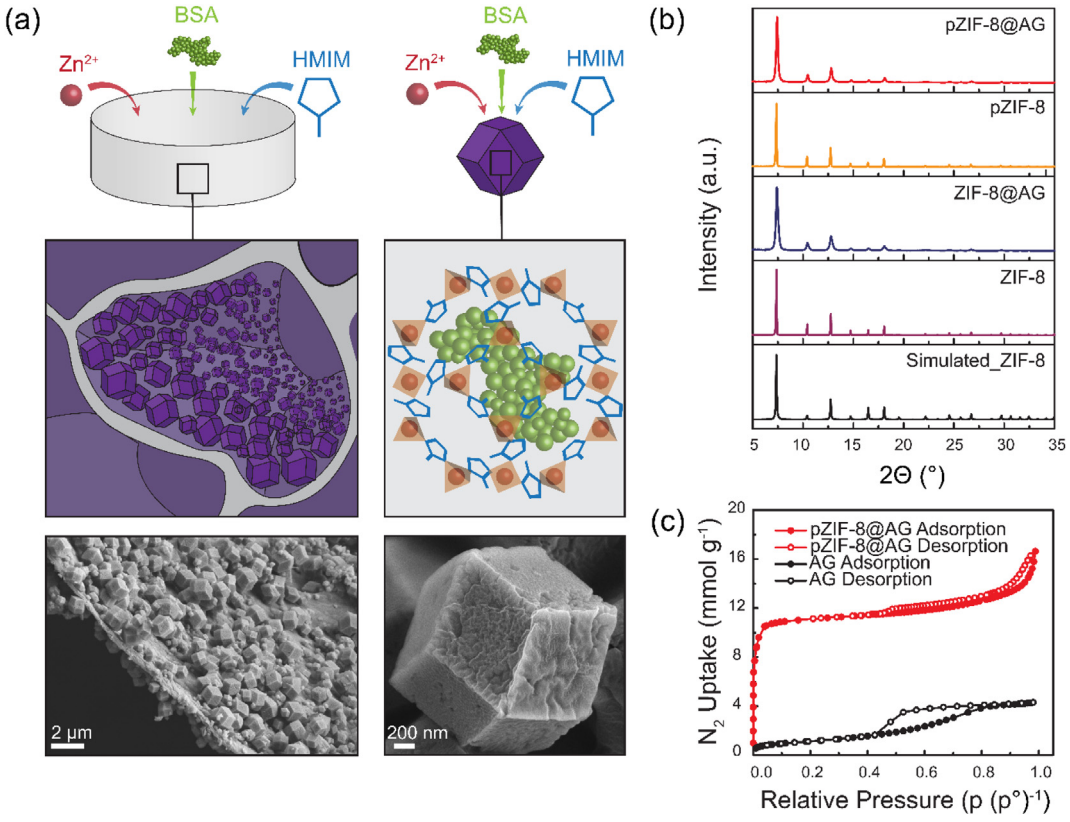

FIGURE 3

MOFs functionalization of AG. Showing (a) schematic description for the formation of protein-containing MOFs (pZIF-8), with or without AG, as well as the respective electron micrographs of the prepared materials, (b) XRD patterns for the MOF functionalized AG aerogels and the MOF powders (c) Gas sorption isotherms for AG aerogels functionalized with protein containing MOFs (pZIF-8@AG) and AG.

Please cite this article in press as: J. Rostami et al., Materials Today (2021), https://doi.org/10.1016/j.mattod.2021.04.013

volume is significantly increased and that the number of pores in the nanometer-range is significantly increased after dissolving the $CaCO_3$ particles, as compared to AG^{Ref} (Fig. S26).

The large SSA of the air-dried AG in combination with their wet stability provides an excellent platform for functionalization of said materials with ZIF-8 MOFs (ZIF-8@AG) or Bovine Serum Albumin (BSA) containing ZIF-8 MOFs (pZIF-8@AG). Moreover, the surface chemistry of the carboxymethylated CNFs is highly advantageous for the *in-situ* growth of MOFs due to the high concentration of carboxylate groups and their affinity towards divalent ions such as Zn^{2+} [59]. Thus, the AG aerogel was first placed in zinc acetate dihydrate solution (120 mM) for 2 h, allowing complete ion exchange to Zn^{2+} (Fig. S27). Following the addition of HMIM solution, with or without BSA, ZIF-8 MOFs with well-defined topologies were obtained, both with and without the AG aerogel present in the solution (Figs. 3a and S28–S29). The high AG surface coverage by the MOFs is supported by a significant weight increase of 139.2 ± 38.7% and 161.3 ± 46.7% for ZIF8@AG and pZIF8@AG, respectively, as well as by the Fourier transform infrared (FTIR) spectroscopy analysis (Fig. S30).

XRD measurements were carried out to further analyze the formation of the MOF structures in solution, as well as on the AG surfaces. As can be seen in Fig. 3b, the signature Bragg peaks for SOD ZIF-8 MOFs are present in all XRD patterns. Additionally, MOFs are known to have high SSA and successful formation and incorporation of the crystals in the AG would result in a significantly larger SSA for the hybrid AG. The results for the functionalized AG indicate high incorporation of MOFs since the SSA of pZIF-8@AG and ZIF-8@AG is 810 and 830 $m^2\ g^{-1}$, respectively (Fig. S31 and Table S7). This is a significant increase if the values are compared with the SSA of the unmodified AG (90 $m^2 g^{-1}$), as seen in the typical adsorption and desorption isotherms of N_2 at 77 K in Fig. 3c. The MOF-functionalized AG aerogels exhibit similar pore size distributions as the MOF powders alone (Fig. S32). Furthermore, they also maintain the wet compression properties, with or without protein incorporation, observed for AG (Fig. S33).

To establish a more detailed localization of BSA, both in solution and on the AG surface, fluorescently-labeled BSA (FBSA) was used in the co-assembly process to prepare the hybrid AG aerogels (fpZIF-8@AG) and MOF powders (fpZIF-8). The presence of the FBSA was evident in both fpZIF-8@AG and fpZIF-8 due to the color change (from white to yellow) of the materials. Indeed, confocal microscopy further showed successful entrapment of the FBSA in the air-dried fpZIF-8 MOFs (Fig. 4a) and fpZIF-8@AG (Fig. 4b).

After successful immobilization of fpZIF-8 MOFs into the AG aerogels (Fig. S34), the hybrid multifunctional materials were soaked in citrate buffer (0.1 M, pH 5.4) and in phosphate buffered saline (PBS, 0.1 M, pH 7.4), respectively, to study the possible controlled release of the FBSA. Fig. 4c shows that the hybrid AG aerogels in pH 5.4 have a controlled release of proteins per gram of encapsulated MOFs, due to the protonation of the HMIM moieties. The figures also show that the control group kept in pH 7.4 indeed displayed minimal release of proteins, in accordance with a previous study [38]. The release experiment was terminated after 150 h, and the hybrid AG aerogel kept in pH 7.4 had maintained its yellow color while the hybrid AG aerogel in pH 5.4 lost more or less all color due to the release of the proteins (Fig. 4d). This is also evident from the color of the surrounding buffer solutions at the start and after 150 h, where the citrate buffer turns yellow with time while the PBS buffer solution remains transparent (Fig. 4e).

The facile biofunctionalization of the AG aerogels with protein-containing MOFs demonstrates the wide potential for these materials to be used as a platform for 3D lightweight bioassays (Fig. 4f). A key step in the development of a sensitive and specific diagnostic assay is the immobilization of biomolecules onto a solid substrate without loss of bioactivity. In addition, the immobilization strategy should provide high loading, control over biomolecule accessibility, and long-term protection from denaturation due to thermal and environmental perturbations [60]. To examine the potential of the hybrid AG as a diagnostic platform, ZIF-8 MOFs were grown on the aerogels with biotinylated BSA (bpZIF-8@AG), following the same approach as described earlier in Fig. 3a. To assess the activity of the bpZIF-8@AG, the material was first soaked in a blocking buffer followed by a washing buffer, to prevent unspecific binding of the detection protein. A horseradish peroxidase (HRP)-conjugated streptavidin was then used for detection of the immobilized protein on bpZIF-8@AG, through a high-affinity binding of biotin to streptavidin [61]. After thoroughly washing, a naked-eye observation of the binding process was achieved after the addition of 3,3′,5,5′-Tetramethylbenzidine (TMB) substrate, which is oxidized by HRP to a blue-colored product on bpZIF-8@AG (Fig. 4g). The controls, i.e. the bare AG, ZIF-8@AG, and pZIF-8@AG, were also subjected to the same protocol. In contrast to bpZIF-8@AG, no obvious visible color change was observed in these control groups (Fig. 4g).

Conclusions

A novel and sophisticated way of making scalable bio-based aerogels under ambient conditions, without any need for energy- and time-consuming procedures, has been demonstrated. By creating a colloidally stable and homogenous network of the selected components (CNFs, alginate, and $CaCO_3$ particles), followed by ice-templating, crosslinking during thawing, and air drying, nanofibrous pore walls were formed that were able to withstand the capillary-force-driven collapse normally observed for this type of network during solvent removal. The resulting air-dried aerogels can have ultra-low densities, favorable specific surface area, a high specific compressive modulus, and excellent wet stability. The applicability as a multifunctional material was demonstrated through a post-functionalization of the aerogels in an all-water-based system to introduce a high loading of protein-containing ZIF-8 MOFs inside the network. As a result of the pH sensitivity of the MOFs, the hybrid materials respond to external stimuli, such as a slight pH change, as demonstrated by the controlled release of immobilized proteins, and thus could be of potential use in controlled-delivery applications. Moreover, biofunctionalization of the 3D lightweight material with high-affinity binding protein enabled a proof-of-concept enzyme-linked immunosorbent assay, which owing to its large specific surface area, is envisioned to have high detection sensitivity.

Please cite this article in press as: J. Rostami et al., Materials Today (2021), https://doi.org/10.1016/j.mattod.2021.04.013

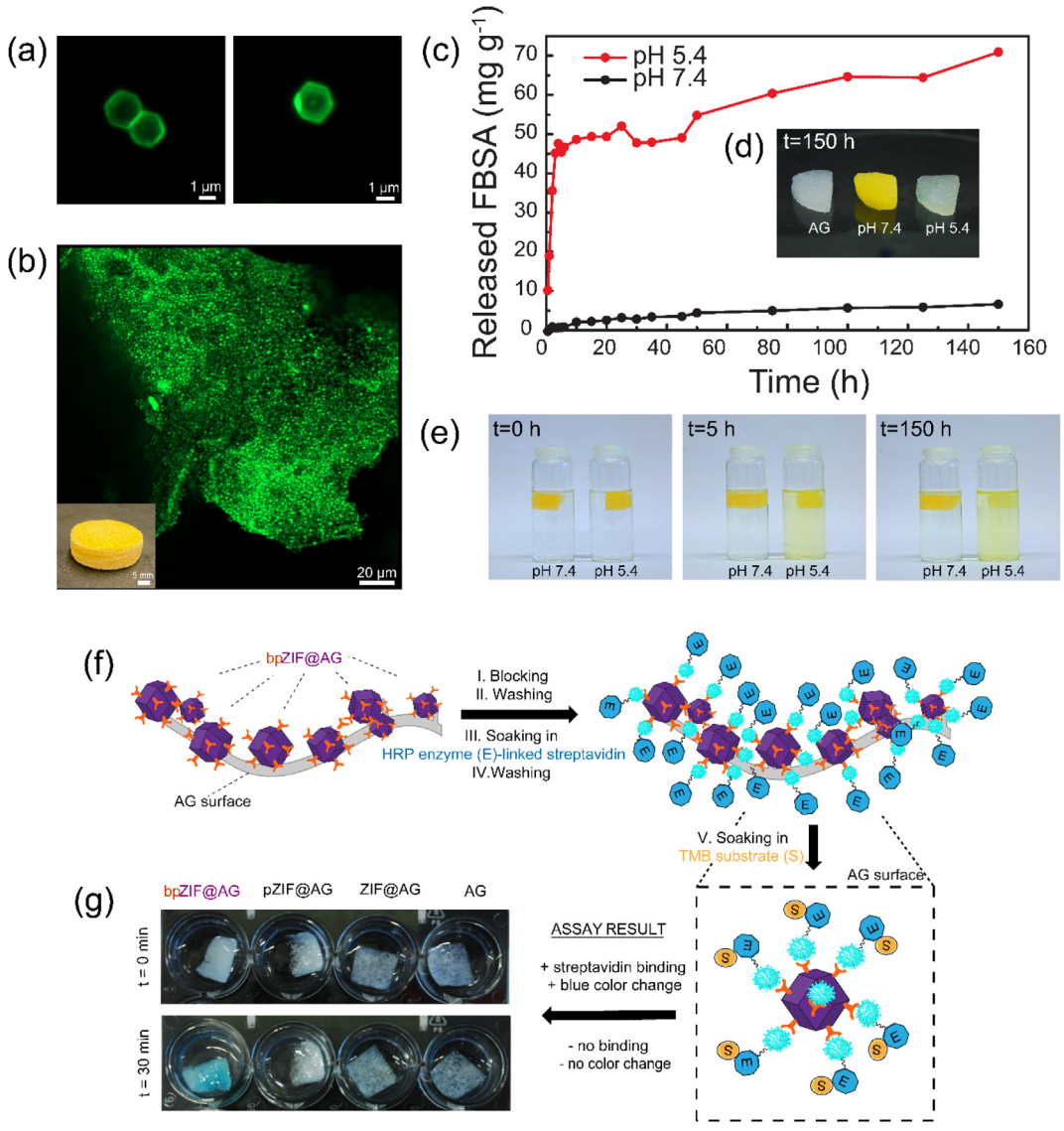

FIGURE 4

Biomimetic MOF functionalized AG with tunable biofunctionality. Showing confocal images of fluorescently-labeled BSA (FBSA) containing MOFs for the (a) powder (fpZIF-8) and (b) hybrid AG (fpZIF-8@AG), (c) the release of FBSA per gram of encapsulated MOFs in citrate buffer (0.1 M, pH 5.4) and phosphate buffered saline (PBS) buffer (0.1 M, pH 7.4), with inset (d) (from left to right) picture of AG in deionized (DI) water, fpZIF-8@AG in pH 7.4 and pH 5.4 after 150 h, and (e) pictures of vials containing the fpZIF-8@AG in the respective pH at different times. (f) Schematic description of the protein binding assay on the hybrid AG for colorimetric detection, using biotinylated BSA (bpZIF-8@AG), and (g) images of bpZIF-8@AG, pZIF-8@AG, ZIF-8@AG, and AG at t = 0 and t = 30 min after soaking in 3,3′,5,5′-Tetramethylbenzidine (TMB) which is oxidized to a blue-colored product by the horseradish peroxidase (HRP) enzyme specifically on bpZIF-8@AG, due to the high-affinity binding and presence of the enzyme (E)-linked streptavidin on the AG aerogel.

Materials and methods

Experimental section

Chemicals

Anhydrous $CaCl_2$, HMIM 99%, sodium chloride (NaCl) ≥ 99.0%, BSA (pH 7.0) ≥ 98.0%, FBSA, sodium citrate tribasic dihydrate ≥ 99.0%, citric acid ≥ 99.5%, Trizma® hydrochloride ≥ 99.0%, HRP-streptavidin, TMB Liquid Substrate System for Enzyme-linked immunosorbent assay (ELISA), PBS (10x, pH 7.2–7.6) and PBS with 0.05% TWEEN® 20 (pH 7.4) were purchased from Sigma-Aldrich (Sweden). Anhydrous sodium carbonate (Na_2CO_3), zinc acetate dihydrate 99.5%, and glacial acetic acid were supplied from Merck (Sweden). Alginic acid sodium salt (high viscosity) was purchased from Alfa Aesar (Germany). Acetone and absolute ethanol were purchased from VWR International. Pierce™ biotinylated BSA and Blocker™ BSA (10X) in PBS were purchased from ThermoFisher Scientific (Sweden). Carboxymethylated CNFs were provided by Rise BioEconomy, (Stockholm, Sweden) as a 2.2% (w/w) hydrogel prepared. All chemicals were used without further purification unless otherwise stated. Merck Milli-Q Ultrapure water (18.2 MΩ/cm) and deionized (DI) water was used throughout all experiments.

Preparation of calcium carbonate particles

To prepare the $CaCO_3$ particle suspension (0.12 M, 100 mL), stock solutions of Na_2CO_3 and $CaCl_2$ were prepared. Firstly, Na_2-

Please cite this article in press as: J. Rostami et al., Materials Today (2021), https://doi.org/10.1016/j.mattod.2021.04.013

CO_3 (1.325 g) and $CaCl_2$ (1.367 g) were each separately dissolved in 50 mL of Milli-Q water and stirred. The Na_2CO_3 solution was added dropwise via a pipette to the $CaCl_2$ solution under vigorous stirring over approximately 15 min, the suspension turned opaque instantly, indicating the formation of sub-micrometer sized $CaCO_3$ particles. The suspension was placed in an ice bath before being homogenized (12 000 rpm, 20 min), using an Ultra-Turrax T25® high-shear mixer from Ika, Staufen, Germany. The suspension was prepared and used on the same day to avoid the formation of larger particle aggregates.

Preparation of carboxymethylated cellulose nanofibrils

Homogenized carboxymethylated CNFs were provided by RISE Bioeconomy, Stockholm, Sweden as a 2.2% (w/w) gel. Upon delivery, the CNFs were homogenized three more times in a Microfluidics MH-110 in 200 μm and 100 μm chambers in series at 1650 bar. The microfluidizer was sterilized with 70% ethanol thrice and then washed with Milli-Q water a further three times before homogenization. The dry content of the obtained gel was calculated by overnight drying of known amounts of gel (105 °C; 5 replicates).

Preparation of sodium alginate solution

The alginate solution was prepared by dissolving high-viscosity alginate in Milli-Q water (0.6% (w/w)) and allowing the solution to stir vigorously overnight. To dissolve the remainder of the gel agglomerates, the solution was placed on an GFL 3015 orbital shaker for an additional day. The solution was then centrifuged (1 h, 6000 rpm) using an Avanti J-E centrifuge from Beckman coulter to remove any undissolved agglomerates, which formed a pellet. The dry content of the obtained solution was calculated by drying known amounts of solution (105 °C; 5 replicates) overnight.

Preparation of aerogels

CNF gel (2.0% (w/w)) and alginate solution (0.51% (w/w)) were mixed in a dry mass ratio of 40:1. The $CaCO_3$ particle suspension (0.12 M, pH 9–10) was then added to the polysaccharide mixture in a 1:6 dry mass ratio. Milli-Q water was added until the final concentration of CNFs, $CaCO_3$ and alginate was 0.90, 0.154, and 0.023% (w/w), respectively. For each replicate, 33 g of the mixture was prepared in centrifuge tubes to keep all parameters the same. The mixtures were homogenized using an Ultra-Turrax high-shear mixer (12 000 rpm, 5 min) and centrifuged (1000 rpm, 5 min), using a Heraeus™ Megafuge™ 8 Small Benchtop Centrifuge, to remove air bubbles. The mixture was aliquoted into polystyrene petri dishes (35 mm wide and 10 mm high, 10 g mixture per mold) and the lids were tightly sealed. The molds were kept in the fridge (4 °C, 1 h) to homogenize the temperature within the dishes before freezing overnight (−18 °C). The following day, each frozen hydrogel (AG) was put in a solution (100 mL/aerogel) of acetic acid (10% (w/w)) in acetone for 1 h at room temperature (RT) before being solvent exchanged with pure acetone (3x15 min, 50 mL/aerogel). The frozen reference hydrogels (AG^{Ref}) were solvent exchanged with pure acetone (3 × 15 min, 50 mL/aerogel) only. All acetone-soaked aerogels were subsequently air-dried. The freeze-dried samples (AG^{FZD}), were freeze-dried directly after the overnight freezing i.e. without any solvent exchange.

In the case of the ultra-light density AG aerogels, the procedure was similar but with the difference that the final concentration of CNFs in the mixtures was 0.12–0.145% (w/w). The frozen hydrogels were also put in acetic acid (10% (w/w)) in acetone for 15 min instead of 1 h, before being air-dried in a desiccator (containing silica beads) with open airflow.

The control groups prepared with $CaCl_2$ instead of $CaCO_3$ followed two different routes. For both control groups, CNFs and alginate were mixed according to the previous dry mass ratio (40:1) with the same final concentrations. The concentration of NaCl present in the $CaCO_3$ dispersion was kept the same for these controls to ensure that the only change was the source of the calcium ions. In the first control group ($AG^{Pre_CaCl_2}$), an equimolar amount of $CaCl_2$ was added to the mixture, instead of $CaCO_3$ particles. The mixture was homogenized with an Ultra-Turrax (12 000 rpm, 5 min), centrifuged for 5 min, put in a freezer overnight (−18 °C) and solvent exchanged with pure acetone (50 mL, 3 × 15 min). The second control group ($AG^{Post_CaCl_2}$) was prepared by freezing CNFs, alginate, and NaCl mixtures. The mixture was solvent exchanged in acetone (containing an equimolar amount of $CaCl_2$, with regards to $CaCO_3$) to post crosslink the network. The samples were put on an orbital shaker to gently mix and assist the dissolution of the $CaCl_2$ while exchanging the solvent. Upon thawing of the aerogels in the acetone, the $CaCl_2$ dissolved. The aerogels were left in the acetone/$CaCl_2$ solution for 1 h, before solvent exchanging to pure acetone (50 mL, 3 × 15 min).

The density of all aerogels was calculated assuming a cylindrical shape. During the freezing step, the lid of the mold is forced upwards; thus, the surface of the frozen hydrogels is uneven and has different heights in different positions. While removing the frozen hydrogels from the molds, some artifacts and material disappearance are also introduced to the edges of the structure. Therefore, the densities for all aerogels were calculated based on an average diameter and average height, with either a caliper or Dino-lite edge 3.0 Digital Microscope.

Preparation of metal organic-framework functionalized aerogels

The AG sample (~0.1 g) was added to a zinc acetate dihydrate solution (pH 6.5, 120 mM, 20 mL) for two hours. Meanwhile, solutions of BSA, FBSA or biotinylated BSA (pH 7, 1 mg/mL, 20 mL) were added with stirring to aqueous HMIM solutions (pH 11.2, 1.92 M). In the control groups, the same volume of DI water, instead of protein solution, was used. The solution was then added to the AG/zinc acetate dihydrate mixture and stirred gently with a magnetic stirrer overnight. The aerogels were first washed under running DI water until the rinsing water became transparent; then twice with Tris-buffered saline (TBS) buffer (pH 7.5, 50 mM Tris-Cl, 150 mM NaCl) before finally being soaked in two absolute ethanol baths with gentle mixing on an orbital shaker. Between each step, the aerogels were sonicated (2 min) using an Elmasonic S 15 ultrasonic bath to remove non-attached crystals from the surfaces. Finally, the hybrid aerogels were left to dry under ambient conditions.

For the control groups without aerogels, all the components above (zinc acetate dihydrate, HMIM, BSA/DI water) with the

Please cite this article in press as: J. Rostami et al., Materials Today (2021), https://doi.org/10.1016/j.mattod.2021.04.013

same concentrations as used above, were mixed in a 1:1:1 volume ratio and left to age for 24 h under static conditions. The MOF dispersions were centrifuged (8700 rpm, 10 min) using a Heraeus™ Megafuge™ 8 Small Benchtop Centrifuge, and the supernatant was discarded. The MOF pellets were then washed by re-suspension and sonication in TBS buffer (pH 7.5, 50 mM Tris-Cl, 150 mM NaCl) and re-pelleted by centrifugation (8700 rpm, 10 min). This was done twice in TBS buffer and then twice in absolute ethanol, sonication was done for 2 min using an Elmasonic S 15 ultrasonic bath. Finally, the MOFs were left to dry under ambient conditions.

Controlled release studies

FBSA was used throughout all controlled-release measurements, where the fluorescence intensity was measured using an Infinite® 200 PRO fluorescent plate reader from Tecan Life Sciences, at excitation 495 nm and emission 525 nm. For the calibration curves, the intensity of different concentrations of FBSA, in either citrate buffer (citric acid and sodium citrate, 0.1 M, pH 5.4) or PBS buffer (0.1 M, pH 7.4), was measured and plotted to establish a linear relationship (Fig. S35).

Four independent fpZIF-8@AG samples were soaked in either 20 mL citrate buffer (0.1 M, pH 5.4) or PBS buffer (0.1 M, pH 7.4). At specified times, 500 μL of the buffer was taken from the vial and replaced with fresh buffer (this dilution was accounted for in subsequent calculations). The average mass of FBSA released was then calculated and normalized to the average amount of encapsulated pZIF-8 in the respective hybrid aerogels.

Colorimetric enzyme-linked detection of high-affinity protein binding on the biofunctionalized aerogels

To demonstrate the applicability of the biofunctionalized aerogels as a 3D bioassay platform, AG aerogels containing biotinylated BSA-incorporated MOFs were prepared (bpZIF-8@AG). Equal masses of bpZIF-8@AG, pZIF-8@AG, ZIF-8@AG, and AG were cut and put in Blocker™ BSA (1X) in PBS solution (1 mL per sample) for 15 min to reduce nonspecific binding. Following this, the samples were placed in a washing buffer (PBS with 0.05% TWEEN® 20, pH 7.4, 15 mL) for 10 min and stirred on an orbital shaker. The samples were placed into 24 well plates containing streptavidin-HRP (1 mL), which had been diluted 1000x with Blocker™ BSA in PBS (1×), and gently shaken for 30 min on an orbital shaker. The samples were washed with washing buffer (3 × 15 min, 15 mL) on an orbital shaker, with 1 min of sonication in between each step, using an Elmasonic S 15 ultrasonic bath. Finally, each sample was immersed in 1 mL of TMB for 30 min to observe the color change from white to blue.

Characterizations

Charge density determination

CNF dispersions of 0.1–0.2% (w/w) were prepared by diluting CNF gel (2% (w/w)) with Milli-Q water, followed by homogenization (12 000 rpm, 20 min) using an Ultra-Turrax high-shear mixer. The dispersions (150–200 mL) were placed in an ice batch and probe sonicated (amplitude 80%, 10 min) using a VCX 750 probe sonicator (diameter 13 mm) from Sonics, followed by centrifugation (4500 rpm, 1 h) using a Mega Star 1.6R centrifuge from VWR. The dry content of the obtained dispersions was calculated by overnight drying of known amounts of dispersions (105 °C, three samples in total). The charge density was determined by polyelectrolyte titration at pH 6–7, using a ParticleMetrix Stabino system. Measurements were performed for three replicates for each dispersion and averaged over all three samples.

Atomic force microscopy

Silica wafers (single-side polished, Addison Engineering Inc. San José, CA, US) were oxidized at 1000 °C for three hours, activated in 10% sodium hydroxide (NaOH) for 30 s, and cleaned in an oxygen plasma (PCD 002, Harrick Scientific Corp., Ossining, NY, US) for two minutes. The wafers were cut into 1 × 1 cm pieces which were dip-coated in branched polyethyleneimine (BPEI, 0.1 g/L, pH 7.5, 1 min) and subsequently CNF dispersions (0.01 or 0.001% (w/w), 1 min). The wafers were imaged using an Atomic Force Microscopy (AFM) MultiMode 8 (Bruker, Santa Barbara, CA, USA) using RTESP-150 cantilevers in either the tapping or the scanAsyst mode.

Zeta potential and size distribution measurements

A $CaCO_3$ suspension was dialyzed for one week under running DI-water to remove NaCl. When the conductivity of the dialyzed material decreased to 57.0 μS cm^{-1} from the pre-dialysis conductivity of 52.0 mS cm^{-1}, the dialyzed $CaCO_3$ was collected and the dry weight was determined. Four different concentrations (0.1, 0.05, 0.01 and 0.005% (w/w)) of dialyzed $CaCO_3$ suspension were prepared and sonicated (5 min) directly before analysis. The ζ-potential was measured three times for each sample, using a Zetasizer Nano ZS from Malvern Instrument Ltd., U.K.

For the size distribution measurements, a non-dialyzed $CaCO_3$ mixture was prepared, diluted 10 times by Milli-Q water, and left to stand at RT for 5 h until clear sedimentation of the larger particles was observed. A sample was taken from the supernatant of the diluted $CaCO_3$ mixture and filtrated through a syringe filter with a mesh size of 1.2 μm, followed by another filtration with a mesh size of 0.2 μm. DLS was used to determine the number-based average particle distribution diameter of the $CaCO_3$ particles. The sample was analyzed three times. Each time, the sample was analyzed with 5 measurements; each measurement consisted of 10 runs with a duration of 10 seconds. The measurement was performed in the optimal position of the cuvette selected by the software.

Scanning electron microscopy and elemental analysis via energy-dispersive X-ray spectroscopy

Aerogels frozen with liquid nitrogen were fractured with a scalpel. Other solutions and suspensions were simply dried and observed as powders. The samples were then mounted onto aluminum stubs, using carbon adhesive tape, and sputter-coated with approximately 5 nm of platinum using a Quorum Q150T ES coater. The morphology of the samples was examined under a Carl Zeiss field-emission Scanning Electron Microscopy (SEM), using secondary electron detectors. Elemental distribution was conducted using an Oxford Instruments' X-Max 80 mm^2 EDS spectrometer.

Please cite this article in press as: J. Rostami et al., Materials Today (2021), https://doi.org/10.1016/j.mattod.2021.04.013

X-ray tomography

X-ray tomography was performed at the 4D-Imaging Lab at the Division of Solid Mechanics, Lund University, Sweden, using a Zeiss XRadia Versa XRM520. For these images, the X-ray tube voltage and power were set to 80 kV and 7 W, respectively. The samples were cut to be 5×5 mm^2 in cross-section and placed 15.08 mm from the source and at 18.82 mm from the detector. 3201 radiographs were acquired over 360° with an exposure time of 1.5 s per projection using 4× optical magnification. The tomographic reconstruction provided a cylindrical image of the internal central section of the sample with both diameter and height of about 2000 voxels, where the voxels are cubic with side lengths of 1.5 μm, giving a field of view of 3 mm in diameter and 3 mm in height. The tomographic reconstruction was performed using the Zeiss reconstructor software with a correction for the center of rotation.

The 3D image volumes from the x-ray tomography were analyzed using Matlab® to separate the aerogel material from the air and to produce an image in which each aerogel cell had a unique label such that measurements of the aerogel morphology could be made (Figs. S9 and S14). For each of the analyzed data sets, the 16-bit tiff images were imported into Matlab® and a central cube of $1301 \times 1301 \times 1301$ voxels was extracted. The image volumes were resampled to reduce the data size and facilitate the processing such that the volumes were $651 \times 651 \times 651$ voxels and the voxel dimensions were halved relative to the original images. Binary volumes were created from the greyscale data by applying a greyscale threshold to separate the solid phase from the air. Subsequently, the individual aerogel cells were separated and labeled by calculating the Euclidean distance map (bwdist) from which local maxima were suppressed (imhmax) due to noise. A topological watershed was applied to the distance map using the Matlab® watershed function after which labeled cells that touched the volume boundary were removed, to avoid partially imaged cells distorting the statistics. Regionprops3 was then used to extract characteristics (Volume, Surface Area, and Principal Axis Length) of the labeled aerogel cells, from which the sphericity was also calculated.

X-ray diffraction

Prior to measurement, aerogels were compressed between two membranes at 23 °C for 20 min at a reduced pressure of 95 kPa using a Rapid Köthen drier (Paper Testing Instruments, Laakirchen, Austria). The MOF-containing aerogels were ground to obtain a fine powder sample for analysis.

The compositions of dry aerogels and powders were evaluated by powder X-ray diffraction, with patterns recorded at room temperature in Bragg-Brentano geometry, using a Panalytical X'Pert PRO MPD and Panalytical X'Pert alpha1 diffractometer (PANalytical, Almelo, Netherlands), operated at 45 kV and 40 mA. Cu Kα was used as the radiation source (λ = 1.540598 Å). The diffraction patterns were recorded with a step size of 0.018°/2θ in the angular range of 5–60°/2θ, with exception for bpZIF-8, bpZIF-8@AG and fpZIF-8@AG that were recorded with a step size of 0.01°/2θ in the angular range of 5–35°/2θ. The compressed porous aerogels or powders were placed on zero-background Si plates in stainless steel sample holders.

The analysis of the peak positions and their identification were performed with the software "HighScore Plus". For comparison, diffractograms of components (NaCl, vaterite, calcite, cellulose and ZIF-8) were simulated using crystallographic information files (cif) files and the "Mercure 4.2.0" software. For cellulose, the peaks in the simulated cif file were broadened as the cellulose used in this project is not a perfect monocrystal, and the particles are of small size, leading to the peaks broadening. For plotting purposes, an arbitrary sample of the replicates was chosen.

Gas sorption

To estimate the specific surface area and pore volume of the materials, sorption of nitrogen at 77 K was performed in an ASAP 2020 (Micromeritics Instrument Corporation, Nocross, USA). For these experiments, unmodified aerogels (∼0.5–1g) and MOF functionalized aerogels (∼100–200 mg) were pressed 2–5 times by hand and cut to smaller pieces to fit them into the narrow round-bottomed tubes. Pure air-dried MOF powders (∼100–200 mg) were placed, as is, into the sample tubes. A filler rod was used to increase the precision of the acquired data. Before the measurement, the samples were degassed for 12–24 h at 70 °C (unmodified aerogels), 80 or 105 °C (MOF functionalized aerogels), and 105 °C (MOF powders) to remove moisture. The specific surface area, pore volume, and pore size distributions were estimated according to BET, BJH, and Density Functional Theory (DFT) models, respectively. With exception for bpZIF-8 and bpZIF-8@AG (due to lack of biotinylated BSA), measurements were performed in duplicates and the BET surface area was averaged over both samples. For plotting purposes, an arbitrary sample of the two replicates was chosen. The BET surface area of the MOFs@AG is highly correlated to the number of MOFs captured within the 3D AG structure, which can vary from sample to sample.

Mechanical analysis

The samples were conditioned for 48 h at 50% relative humidity, and the mass was recorded to measure the moisture sorption. Dimensions of the aerogels were measured either before or after conditioning since no significant difference in sample volume before or after conditioning was observed in previous measurements. For evaluating the wet mechanical properties, the samples were fully wetted with Milli-Q water for at least 1 h (after the 48 h of conditioning). The dry and wet mechanical properties were evaluated under compression, using an Instron 5944 equipped with a 500 N load cell. The load rate was 10%/min (a typical sample has a diameter of 27–33 mm and a height of 8–12 mm) and the samples were compressed until 90% or 80% for the dry or wet state, respectively. The compression was started at the maximum point of the aerogel registered by the tool, in both dry and wet states, due to the unevenness of the sample surface. Thus, the stress–strain curve shows some non-linearity at the beginning. For all aerogels, the compression modulus was calculated for the steepest region (before yielding of the sample), to avoid the starting region where full contact was not yet established. The compressive modulus for each specimen, including the control groups, was then normalized to its post-conditioned density, assuming a cylindrical form of the aerogel.

Please cite this article in press as: J. Rostami et al., Materials Today (2021), https://doi.org/10.1016/j.mattod.2021.04.013

For the wet samples, the shape recovery was measured for all cycles and averaged over two samples for each cycle. For plotting purposes, an arbitrary sample of the replicates was chosen.

Fourier transform infrared spectroscopy

A PerkinElmer Spectrum 2000 FTIR, equipped with an attenuated total reflection (ATR) Golden Gate from Graseby Specac (Kent, UK) was used to record FTIR spectra. All spectra were attained in the spectral region of 4000–600 cm^{-1}, with a spectral resolution of 4 cm^{-1} and 64 scans. Carbon dioxide and atmospheric water were corrected for by a background scan before each sample. All spectra were measured by transmittance and converted to absorbance as followed: absorbance = 2 − log(%T). For plotting purposes, an arbitrary sample of the replicates was chosen.

Confocal microscopy

The presence of the FBSA was determined using the confocal laser scanning microscopy (CLSM) technique (Confocal Microscope Zeiss LSM 800 Airyscan) with the following objectives: Plan-Apo 63x/1.40NA Oil, Plan-Neofluar 10x/0.35NA, and Fluar 5X/0.25NA for an overview. The FBSA was excited at 488 nm and the signal was collected between 450–700 nm using the Airyscan detector. Images are shown after "Airyscan" image processing.

Data availability

Experimental data from this study are available from the corresponding author upon reasonable request.

CRediT authorship contribution statement

Jowan Rostami: Conceptualization, Methodology, Software, Validation, Formal analysis, Investigation, Data curation, Writing - original draft, Visualization, Supervision, Project administration. **Korneliya Gordeyeva:** Methodology, Investigation, Writing - review & editing. **Tobias Benselfelt:** Investigation, Visualization, Validation, Writing - review & editing. **Ekeram Lahchaichi:** Investigation, Writing - review & editing. **Stephen Hall:** Methodology, Investigation, Formal analysis, Writing - review & editing. **Anastasia V. Riazanova:** Resources, Writing - review & editing. **Per A. Larsson:** Validation, Writing - review & editing, Supervision. **Goksu Cinar Ciftci:** Conceptualization, Methodology, Validation, Investigation, Writing - review & editing, Supervision. **Lars Wågberg:** Conceptualization, Methodology, Validation, Resources, Writing - review & editing, Supervision, Project administration, Funding acquisition.

Declaration of Competing Interest

The authors declare that they have no known competing financial interests or personal relationships that could have appeared to influence the work reported in this paper.

Acknowledgments

JR acknowledges VR, the Swedish Research Council, for financial support and LW acknowledges the Knut and Alice Wallenberg Research Foundation, via WWSC, for financial support. The authors acknowledge the Treesearch organization for financial support and the facilities and technical assistance of Cheng Choo Lee at the Umeå Core Facility Electron Microscopy (UCEM), Umeå University and the National Microscopy Infrastructure (NMI). The tomography analysis (SH) was in part supported by the QIM project at Lund University. The authors would also like to thank Miscible Text for proofreading the language of the manuscript and Andrew Marais for contributing photographs.

Conflict of Interest

The authors declare no conflict of interest.

Appendix A. Supplementary data

Supplementary data to this article can be found online at https://doi.org/10.1016/j.mattod.2021.04.013.

References

[1] A.D. McNaught, A. Wilkinson, Compendium of Chemical Terminology, Blackwell Science, Oxford, 1997.
[2] T. Gao et al., Constr. Build. Mater. 52 (2014) 130.
[3] B. Wicklein et al., Nat. Nanotechnol. 10 (2014) 277.
[4] F. Jiang, Y.-L. Hsieh, J. Mater. Chem. A 2 (18) (2014) 6337.
[5] H. Zhu et al., Adv. Mater. 28 (35) (2016) 7652.
[6] J. Choi, D.J. Suh, Catal. Surv. Asia 11 (3) (2007) 123.
[7] G. Pajonk, Catal. Today 35 (3) (1997) 319.
[8] G. Nyström et al., Nat. Commun. 6 (2015) 7259.
[9] S.C. Li et al., Angew. Chem. Int. Ed. 57 (24) (2018) 7085.
[10] S.S. Kistler, Nature 127 (3211) (1931) 741.
[11] T. Benselfelt et al., Adv. Mater. Interfaces 6 (13) (2019) 1970085.
[12] A.B. Fall et al., Langmuir 27 (18) (2011) 11332.
[13] J. Erlandsson et al., Biomacromolecules 20 (2) (2018) 728.
[14] Y. Li et al., ACS Sustainable Chem. Eng. 5 (8) (2017) 6387.
[15] J. Erlandsson et al., J. Mater. Chem. A 6 (40) (2018) 19371.
[16] H. Françon et al., Adv. Funct. Mater. 30 (12) (2020) 1909383.
[17] T. Benselfelt, L. Wågberg, Biomacromolecules 20 (6) (2019) 2406.
[18] K.J. De France et al., Chem. Mater. 29 (11) (2017) 4609.
[19] S. Sultan et al., Adv. Funct. Mater. 29 (2) (2019) 1805372.
[20] L. Zhu et al., ACS Nano 12 (5) (2018) 4462.
[21] S. Furukawa et al., Chem. Soc. Rev. 43 (16) (2014) 5700.
[22] G. Maurin et al., Chem. Soc. Rev. 46 (11) (2017) 3104.
[23] H. Furukawa et al., Science 341 (6149) (2013) 1230444.
[24] K.S. Park et al., Proc. Natl. Acad. Sci. 103 (27) (2006) 10186.
[25] M.S. Denny et al., Nat. Rev. Mater. 1 (12) (2016) 1.
[26] H. Li et al., Mater. Today 21 (2) (2018) 108.
[27] F.R. Fortea-Pérez et al., Nat. Mater. 16 (7) (2017) 760.
[28] R.B. Lin et al., Adv. Sci. 3 (7) (2016) 1500434.
[29] Y. Yang et al., RSC Adv. 6 (51) (2016) 45475.
[30] H.N. Abdelhamid et al., Microchim. Acta 184 (9) (2017) 3363.
[31] O. Karagiaridi et al., J. Am. Chem. Soc. 134 (45) (2012) 18790.
[32] Q. Bao et al., Inorg. Chem. Commun. 37 (2013) 170.
[33] K. Kida et al., CrystEngComm 15 (9) (2013) 1794.
[34] S. Watanabe et al., Chem. Eng. J. 313 (2017) 724.
[35] W. Liang et al., Chem. Mater. 30 (3) (2018) 1069.
[36] O. Kolmykov et al., Mater. Des. 122 (2017) 31.
[37] X.C. Huang et al., Angew. Chem. Int. Ed. 45 (10) (2006) 1557.
[38] K. Liang et al., Nat. Commun. 6 (2015) 7240.
[39] J. Huo et al., Chem. Sci. 6 (3) (2015) 1938.
[40] K. Liang et al., Chem. Commun. 52 (3) (2016) 473.
[41] Y. Feng et al., Adv. Mater. 31 (2) (2019) 1805148.
[42] C. Doonan et al., Acc. Chem. Res. 50 (6) (2017) 1423.
[43] L. Kocon et al., J. Non-Cryst. Solids 225 (1998) 96.
[44] T. Tillotson, L. Hrubesh, J. Non-Cryst. Solids 145 (1992) 44.
[45] G. Hayase et al., Chem. Mater. 27 (1) (2015) 3.
[46] J. Zou et al., ACS Nano 4 (12) (2010) 7293.
[47] Z.Y. Wu et al., Angew. Chem. 125 (10) (2013) 2997.
[48] M.M. Biener et al., Adv. Mater. 26 (28) (2014) 4808.
[49] T. Benselfelt et al., Green Chem. 20 (11) (2018) 2558.
[50] M. Abebe et al., Cryst. Growth Des. 15 (8) (2015) 3609.
[51] A. Yashchenok et al., J. Mater. Chem. B 1 (9) (2013) 1223.

Please cite this article in press as: J. Rostami et al., Materials Today (2021), https://doi.org/10.1016/j.mattod.2021.04.013

[52] A.A. Antipov et al., Colloids Surf, A 224 (1–3) (2003) 175.
[53] T. Benselfelt et al., Adv. Mater. Interfaces 6 (13) (2019) 1900333.
[54] H. Sehaqui et al., Soft Matter 6 (8) (2010) 1824.
[55] T. Benselfelt, L. Wagberg, Biomacromolecules 20 (6) (2019) 2406.
[56] Y. Kobayashi et al., Angew. Chem. Int. Ed. 53 (39) (2014) 10394.
[57] J. Erlandsson et al., Biomacromolecules (2018).
[58] L. Geng et al., Macromolecules 51 (4) (2018) 1498.
[59] T. Benselfelt et al., Nanoscale 11 (8) (2019) 3514.
[60] C. Sicard, J.D. Brennan, MRS Bulletin 38 (4) (2013) 331.
[61] P. Vincent, D. Samuel, J. Immunol. Methods 165 (2) (1993) 177.

Please cite this article in press as: J. Rostami et al., Materials Today (2021), https://doi.org/10.1016/j.mattod.2021.04.013